This is the Pre-Published Version.

This version of the article has been accepted for publication, after peer review (when applicable) and is subject to Springer Nature's AM terms of use, but is not the Version of Record and does not reflect post-acceptance improvements, or any corrections. The Version of Record is available online at: http://dx.doi.org/10.1038/s41563-021-01001-7.

Wafer-scale growth of large-area few-layer two-dimensional black phosphorus

Authors: Zehan Wu[1,2], Yongxin Lyu[1,2], Yi Zhang[1], Ran Ding[1], Beining Zheng[1], Zhibin Yang[1], Shu Ping Lau[1], Xian Hui Chen[3] * and Jianhua Hao[1,2] *

Affiliations:

[1]Department of Applied Physics, The Hong Kong Polytechnic University, Hung Hom, Hong Kong, P.R. China.

[2]The Hong Kong Polytechnic University Shenzhen Research Institute, Shenzhen 518057, P. R. China.

[3]Hefei National Laboratory for Physical Sciences at Microscale and Department of Physics, and CAS Key Laboratory of Strongly-coupled Quantum Matter Physics, University of Science and Technology of China, Hefei, Anhui 230026, P.R. China.

*Correspondence authors: chenxh@ustc.edu.cn; jh.hao@polyu.edu.hk.

The development of information industry based on conventional semiconductors is confronted with a huge barrier since the silicon-chip technology is about to reach the physical limit. Instead, two-dimensional (2D) materials provide new opportunities for developing semiconductor applications at atomistic thickness. However, graphene lacks the energy bandgap (E_g), while other 2D semiconductors do not possess sufficiently high mobility, fundamentally hindering them from being the key material for transistor devices. Black phosphorus (BP), as a layered semiconductor with controllable bandgap and high carrier-mobility, is the most promising candidate for transistor devices at atomistic thickness[1-4]. However, among main 2D-materials, BP is the only one left that wafer-scale growth has not been realized, greatly hindering its device development. Here we report the wafer-scale growth of ultra-thin BP for the first time via pulsed laser deposition (PLD). The unique plasma-activated region induced by laser ablation provides highly desirable conditions for BP-cluster formation and transportation, facilitating the growth of few-layer BP in centimeter scale[5-6]. Furthermore, we fabricate BP-based wafer-scale field-effect-transistor (FET) arrays, yielding appealing hole-mobility up to 213 and 617 $cm^2V^{-1}s^{-1}$ at 295 and 250 K, respectively. Our results pave the way for developing BP-based wafer-scale device applications, which is of significance for future information industry.

BP, a re-discovered elemental 2D semiconductor, possesses both appealing carrier-mobility and widely tunable bandgap from 0.3 eV in bulk to around 2 eV for monolayer[7], covering the magnitudes of E_g from conventional semiconductors for transistor devices (e.g. $E_{g,Si}$~1.12 eV, $E_{g,GaAs}$~1.44 eV). Moreover, BP exhibits various unique properties, which are valuable for broad applications ranging from nano-electronics and -photonics to quantum devices and superconductor[7-12]. Putting them together makes BP an ideal candidate for 2D applications, which will finally break through development obstacles and lay the foundation for 2D materials in information industry. Contrary to its significant application prospects, the controllable wafer-scale growth of few-layer BP films has been a long-standing major problem since the discovery of BP, and the lack of solution has greatly hindered its further investigations and practical applications. To date, the top-down exfoliated BP suffers from its limited scale and irregular shape, besides which the red-phosphorus-based allotropic-transformation approach cannot form high-quality films with atomistic thickness[11-13]. Recently, chemical vapor deposition (CVD) enabled bottom-up synthesis of BP, but only flakes up to dozens of micrometers in lateral scale are obtained[14,15]. This is due to the unique sp^3 hybridization of P atoms in BP, which results in a relatively high surface-energy than the substrate, hindering the lateral layer-growth of BP[6]. Besides, the construction of BP phase requires extreme high-pressure condition, which can hardly be achieved in those vapor-phase deposition approaches[7]. Here we report a controlled PLD strategy to synthesize high-quality few-layer BP in wafer scale. In combination with molecular dynamic (MD) simulations, we show that, instead of conventional heat-assisted evaporation, the

54 employment of pulsed-laser can facilitate the formation of large BP-clusters within the
55 transported physical-vapor, thus significantly reduces the formation energy of BP phase
56 and enables the wafer-scale growth of few-layer BP[5-6]. In addition to demonstrations
57 on the large-area crystalline-homogeneity of the obtained BP, we move forward to
58 fabricate BP-film-based wafer-scale FET-arrays, exhibiting appealing electrical
59 performances that are not only comparable to those of previously reported BP in only
60 micrometer scale, but also highly uniform over entire film in centimeter scale, setting
61 the crucial stage for BP-based semiconductor integrated-circuits in information industry.
62
63 We achieved the wafer-scale BP growth in an ultrahigh-vacuum chamber by using bulk
64 mono-crystal BP as source and mica with freshly exfoliated surface as substrate (Fig.
65 1a, see also Methods and Extended Data Fig. 1). Different reflective color in contrast
66 to the bare mica can be observed for the as-grown BP films (Fig. 1b), and the uniform
67 sheen extends over the 1-cm^2 surface of mica substrate, signifying great potential for
68 subsequent wafer-scale device-array fabrications. Additionally, precise control of the
69 film thickness (i.e. the layer number) is readily achieved via manipulating the number
70 of laser-pulses during deposition, and a growth rate of ~1.3 Å/s is deduced (Extended
71 Data Fig. 2). Contributing to the homogeneous distribution and high density of BP
72 clusters in laser-generated physical-vapor, the growth and merging of monolayered BP
73 flakes are thermo-dynamically preferred, facilitating the formation of a continuous film
74 (Fig. 1 c-e and Extended Data Fig. 3). Fig. 1f exhibits the X-ray diffraction (XRD)
75 results of the obtained film, where three main diffraction peaks of (0 2n 0) can be

recognized in addition to the patterns of mica substrate. This fingerprint corresponds to the typical orthorhombic structure of BP crystal[16], which further confirms the high crystallinity of as-prepared large-area BP films.

The key idea in our process is to make use of the extreme high-temperature and high-pressure conditions within the confined region created by the plasma cloud to fulfill energetic BP-cluster formation and transportation during the non-equilibrium process of PLD (Extended Data Fig. 4 and Supplementary Video). To gain theoretical insights into the growth mechanism, we conducted MD simulations on the formation of BP clusters. The simulation results show that the temperature and pressure within laser-generated plasma-cloud can reach higher than 10^3 K and 10^9 Pa, respectively, which are highly desirable for BP-clusters formation[6,7]. Fig. 1 g-h show the radial distribution functions (RDF) obtained from MD simulations under various laser-fluence. As indicated by four characteristic peaks of the interatomic interactions in BP structure[17,18], the formation of BP clusters is likely to happen within the high-pressure region created by low-energy pulsed-laser (Extended Data Fig. 5, see also Methods), thus facilitating the subsequent growth of BP films. Accordingly, such a laser-activated physical vapor deposition (PVD) differing from conventional CVD and other PVD techniques has proved to be a feasible and powerful tool for the growth of wafer-scale few-layer BP films based on our exploration.

Owing to the characteristic lattice vibration of BP, the continuity and homogeneity of

BP films can be verified by Raman mapping, especially the anisotropic features of A^2_g peak[13,19,20]. Fig. 2 a-b and Extended Data Fig. 6 show the large-area Raman-mapping investigations on the as-grown BP film, demonstrating high homogeneity of BP-lattice vibration. We therefore conclude that the BP films obtained by our process have identical crystal-orientation within large area. As further evidences, polarized Raman measurements were performed on five randomly selected positions of the sample, where similar angle-dependent anisotropic features were observed (Extended Data Fig. 6c). Additionally, layer-dependent Raman and photoluminescence (PL) performance can also be observed (Fig. 2 c-d), while the identical E_g is also verified via PL line-scan mapping (Fig. 2e), further evidencing the film uniformity and implying the controllable layer-by-layer growth[17,21].

It is worth noting that surface ripples oriented along similar direction are visible within large area (Fig. 3a), which have been reported to be highly dependent on the BP-crystal orientation[13], Hence, it is reasonable to speculate that our BP films possess high crystalline-homogeneity. To further investigate the microscopic crystal-structure, high-resolution transmission electron microscope (HR-TEM) studies were performed. Fig. 3b exhibits the plan-view image of a ~8-layer BP, verifying the highly ordered arrangement of BP atoms without visible particulate incorporated to the as-grown film. The corresponding energy-dispersive X-ray spectroscopy (EDX) spectrum and element-mapping image under high-angle annular dark-field (HAADF) measurement were shown in Fig. 3 c-d, from which the elemental purity of as-prepared BP film is

evidenced and potential contaminations such as oxidized species can be ruled out. Fig. 3e illustrates a detailed HR-TEM image showing typical atomic-arrangement pattern corresponding to the orthorhombic structure of BP crystal. Lattice spacing of 3.30 and 4.55 Å can be extracted along zigzag and armchair directions, respectively, which match well with the lattice constants of BP[16]. The inserted ball-stick schematic diagrams illustrate the atom arrangement of AB stacking structure of adjacent BP layers[22]. The corresponding selected-area electron diffraction (SAED) patterns are shown in Fig. 3f, from which a typical orthogonal lattice with homologous quadruple symmetry can be concluded, highly indicative of the crystalline nature of as-prepared sample.

The longitudinal interlaminar structure of the obtained BP films with various layer-number was studied by cross-sectional TEM (Fig. 3 g-h), where the well-defined layer structure can be recognized. We calculated the spacing between neighboring BP-layers to be ~0.53 nm, which is consistent with the well-accepted BP-lattice spacing of ~0.52-0.56 nm[23]. Specifically, the unique double-atom-layer characteristic of BP monolayer can be observed, and distinct stratification of mica substrate and each BP layer can be recognized via the van der Waals (vdW)- vacuum layers. Further TEM investigations (Extended Data Fig. 7) suggest that deteriorations may gradually occur on the bottom BP-layers while the upper BP-layers continue to grow, which should be attributed to the random deformation and shifting of BP layers happening under high temperature[24,25]. Since a relatively high temperature of ~300 ℃ is required for the lateral growth of BP

films, we adopted a rapid-cooling strategy after deposition to overcome such obstacles (Extended Data Fig. 1-2), and the obtained large-area few-layer BP films are just adequate to satisfy further evolution of wafer-scale applications at atomistic thickness.

FET is the most used device to test electrical performance of semiconductors. Benefiting from the considerable crystalline-size of as-grown BP, we fabricated FETs using hard-mask-based electron-beam deposition technology, which allows readily construction of electric devices to avoid possible contamination or oxidation. As shown in Fig. 4 a-b, 10-nm-Pd/40-nm-Au multi-layer was used as electrodes. Notably, palladium was employed as an adhesion layer due to its good electrical conductivity and decent welding-performance during construction process in activated ionic-liquid, as well as suitable work-function accompanying the Fermi energy of BP. Fig. 4c shows the gate-voltage-modulated current-voltage (*I*-*V*) output characteristics, from which linear correlation can be concluded for the Ohmic-contact between electrodes and BP layers. Further field-effect transfer performance was studied by utilizing ionic liquid as gate dielectric, from which the typical p-type transferring behaviors with excellent electrical performances in terms of field-effect hole-mobility (μ_H) and current-switching ratio were obtained (Fig. 4d, see more details in Extended Data Fig. 8-9). It is worth noting that BP samples with the thickness below or above ~5 nm possess different electrical performance (Fig. 4e). For the samples thinner than 5 nm, a linear proportional relationship between carrier mobility and film thickness is observed. The promotion of carrier mobility can be attributed to the narrowed bandgap of ultrathin BP

layers, in accordance with previous studies on other semiconductors[26]. Besides, the scattering and screening effects of impurities in layered materials may also contribute to this thickness-dependent phenomenon[2]. In contrast, as the sample thickness exceeds 5 nm, a cliff-like drop of the carrier mobility emerges. Considering that the inhibition of interlayer coupling is unlikely to produce such a significant effect in ultrathin films, the decrease of carrier mobility is therefore attributed to the deterioration of crystalline quality in thicker BP samples, as verified by the observed defects such as dislocation and grain boundaries under TEM. For current switching ratio, a similar trend is observed with an inflection point at 5 nm. The downtrend for the films thinner than 5 nm is mainly due to the 2D nature of ultrathin films, that is, the modulation ability of gate voltage tends to be suppressed usually for thicker layers[1]. On the other hand, as the film thickness exceeds 5 nm, the deterioration of crystalline quality starts to affect the ON-current, causing a steeper slope of the curve. Among all samples, ~5-nm-thick BP films exhibit optimal performance of field-effect electrical transfer properties, and the carrier mobility reaches ~617 $cm^2V^{-1}s^{-1}$ at 250 K. The obtained electrical characteristics are comparable to those exfoliated or CVD-grown BP-based FETs with similar thickness (Extended Data Fig. 9 and Table 1). Notably, compared with those limited-scale BP flakes in earlier reports, our centimeter-scale BP films exhibit highly uniform electrical-performance, as indicated by carrier-mobility mapping result from 25 different locations on the wafer (Fig. 4f). This is of high significance in breaking through the scalable-application obstacles to lay the foundation for BP industrialization in information industry.

In summary, we have presented controllable and rapid PLD process to directly synthesize few-layered BP in centimeter-scale with high crystalline-quality and homogeneity. Combined with MD simulations, the growth mechanism of forming BP layer is understood. We have investigated the crystal phase, crystalline quality, layered structure, and energy bandgap of as-prepared large-area BP films. Followed by the success of growing large-area BP, we further fabricated few-layer BP FETs. The wafer-scale-grown BP device-array exhibits appealing electrical characteristics in terms of carrier mobility and current switching ratio, which are comparable even exceeding to those of previously reported exfoliated or chemically grown BP flakes with similar thickness but much smaller scale (Extended Data Table 1). Hence, this report is the first time to demonstrate large-area growth of few-layer BP whose size is significantly increased from dozens of micrometers available to centimeter. It is worth noting that PLD enjoys attractive features beneficial to wafer-scale device fabrications including well-controllable thickness, stoichiometry growth, fast growth-rate, and high compatibility with making multi-layered heterostructure simply via rotating multiple targets without breaking vacuum. In contrast to much smaller sized BP flakes fabricated by other approaches, our work opens up the possibility of developing BP-based wafer-scale electronic and optoelectronic devices, especially scalable integrated device-array and information system.

References

1 Li, L. *et al.* Black phosphorus field-effect transistors. *Nat. Nanotechnol.* **9**, 372-377 (2014).

2 Qiao, J., Kong, X., Hu, Z. X., Yang, F., & Ji, W. High-mobility transport anisotropy and linear dichroism in few-layer black phosphorus. *Nat. Commun.* **5**, 4475 (2014).

3 Xia, F., Wang, H. & Jia, Y. Rediscovering black phosphorus as an anisotropic layered material for optoelectronics and electronics. *Nat. Commun.* **5**, 4458 (2014).

4 Liu, H. *et al.* Phosphorene: An Unexplored 2D Semiconductor with a High Hole Mobility. *ACS Nano* **8**, 4033-4041 (2014).

5 Lowndes, D. H., Geohegan, D. B., Puretzky, A. A., Norton, D. P., & Rouleau, C. M. Synthesis of novel thin-film materials by pulsed laser deposition. *Science* 273, 898-903 (1996)

6 Shriber, P., Samanta, A., Nessim, G. D. & Grinberg, I., First-principles investigation of black phosphorus synthesis. *J. phys. Chem. Lett.* **9**, 1759-1764 (2018)

7 Liu, H., Du, Y., Deng, Y. & Ye, P. D. Semiconducting black phosphorus: synthesis, transport properties and electronic applications. *Chem. Soc. Rev.* **44**, 2732-2743 (2015).

8 Wang, X. *et al.* Highly anisotropic and robust excitons in monolayer black phosphorus. *Nat. Nanotechnol.* **10**, 517-521 (2015).

9 Youngblood, N., Chen, C., Koester, S. J. & Li, M. Waveguide-integrated black phosphorus photodetector with high responsivity and low dark current. *Nat. Photonics* **9**, 247-252 (2015).

10 Wu, Z. & Hao, J. Electrical transport properties in group-V elemental ultrathin 2D layers. *NPJ 2D Mater. Appl.* **4**, 1-13 (2020).

11 Chen, L. *et al.* Scalable Clean Exfoliation of High-Quality Few-Layer Black Phosphorus for a Flexible Lithium Ion Battery. *Adv. Mater.* **28**, 510-517 (2016).

12 Hanlon, D. *et al.* Liquid exfoliation of solvent-stabilized few-layer black phosphorus for applications beyond electronics. *Nat. Commun.* **6**, 8563 (2015).

13 Li, C. *et al.* Synthesis of Crystalline Black Phosphorus Thin Film on Sapphire. *Adv. Mater.* **30**, 1703748 (2018).

14 Smith, J. B., Hagaman, D. & Ji, H. F. Growth of 2D black phosphorus film from chemical vapor deposition. *Nanotechnology* **27**, 215602 (2016).

15 Xu, Y. *et al.* Epitaxial nucleation and lateral growth of high-crystalline black phosphorus films on silicon. *Nat. Commun.* **11**, 1330 (2020).

16 Castellanos-Gomez, A. *et al.* Isolation and characterization of few-layer black phosphorus. *2D Mater.* **1**, 025001 (2014).

17 Sha, W., Wu, X. & Keong. K. G., *ELECTROLESS COPPER AND NICKEL-PHOSPHORUS PLATING* Ch. 6. Molecular dynamics (MD) simulation of the diamond pyramid structure in electroless copper deposits, (Woodhead publishing, Cambridge, 2011).

18 Brown, A. & Rundqvist, S. Refinement of the crystal structure of black

phosphorus. *Acta Cryst.* **19**, 684-685 (1965).

19 Zhang, S. *et al.* Extraordinary Photoluminescence and Strong Temperature/ Angle-Dependent Raman Responses in Few-Layer Phosphorene. *ACS Nano* **8**, 9590-9596 (2014).

20 Guo, Z. *et al.* From Black Phosphorus to Phosphorene: Basic Solvent Exfoliation, Evolution of Raman Scattering, and Applications to Ultrafast Photonics. *Adv. Funct. Mater.* **25**, 6996-7002 (2015).

21 Favron, A. *et al.* Photooxidation and quantum confinement effects in exfoliated black phosphorus. *Nat. Mater.* **14**, 826-832 (2015).

22 Lei, S., Wang, H., Huang, L., Sun, Y. Y. & Zhang, S. Stacking Fault Enriching the Electronic and Transport Properties of Few-Layer Phosphorenes and Black Phosphorus. *Nano Lett.* **16**, 1317-1322 (2016).

23 Morita, A. Semiconducting Black Phosphorus. *Appl. Phys. A* **39**, 227-242 (1986).

24 Lin, S. *et al. In situ* observation of the thermal stability of black phosphorus. *2D Mater.* **4**, 025001 (2017).

25 Liu, X., Wood, J. D., Chen, K. S., Cho, E. & Hersam, M. C. In Situ Thermal Decomposition of Exfoliated Two-Dimensional Black Phosphorus. *J. Phys. Chem. Lett.* **6**, 773-778 (2015).

26 Schwierz, F. Graphene transistors. *Nat. Nanotechnol.* **5**, 487-496 (2010).

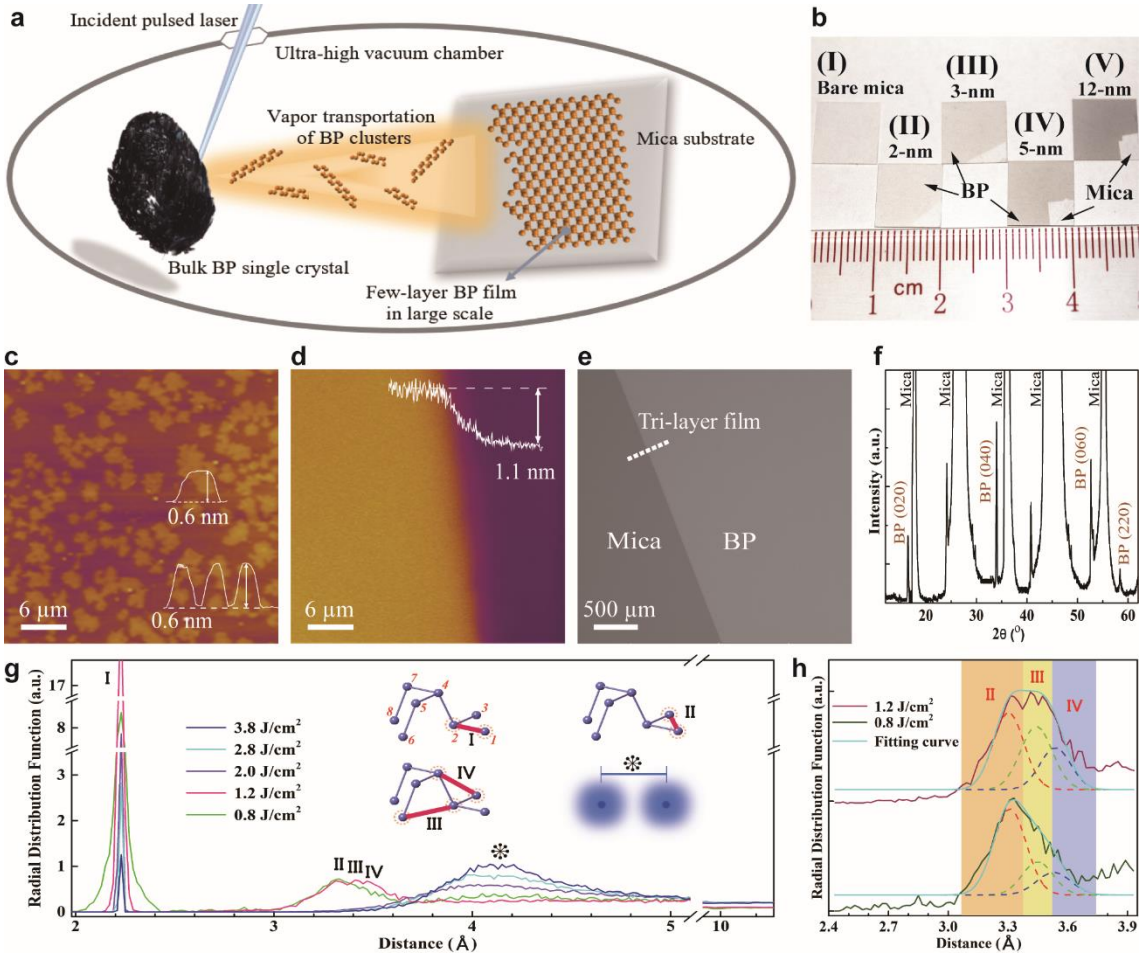

Fig. 1 Wafer-scale growth of few-layer BP films. a, Schematic of controlled PLD process for few-layer BP film fabrication. **b,** Photographs of bare mica substrate (I) and as-deposited centimeter-scale BP films with different thickness (II-V), respectively. **c,** atomic force microscope (AFM) image showing the topography of monolayer BP flakes synthesized with a few laser pulses. The monolayer thickness is indicated by the inserted height profile. **d,** AFM images indicating the thicknesses of a bilayer BP film. **e,** Electron back scatter (EBS) image of a tri-layer BP film on mica substrate showing the uniformity and continuity surpassing millimeter scale. **f,** XRD spectrum of as-synthesized BP. Peaks corresponding to typical orthorhombic structure of BP are dominant. **g,** RDF curves extracted from MD simulation with varying laser fluence. Four characteristic peaks (*I-IV*) are responsible for the fingerprints of BP allotrope, which renders the distinction between different phosphorus allotropes. The flat peak centered at ~4.15 Å represents vdW-interaction between P atoms without chemical. Differentiation and imitating of the broad peaks centered at ~3.40 Å are shown in **h**.

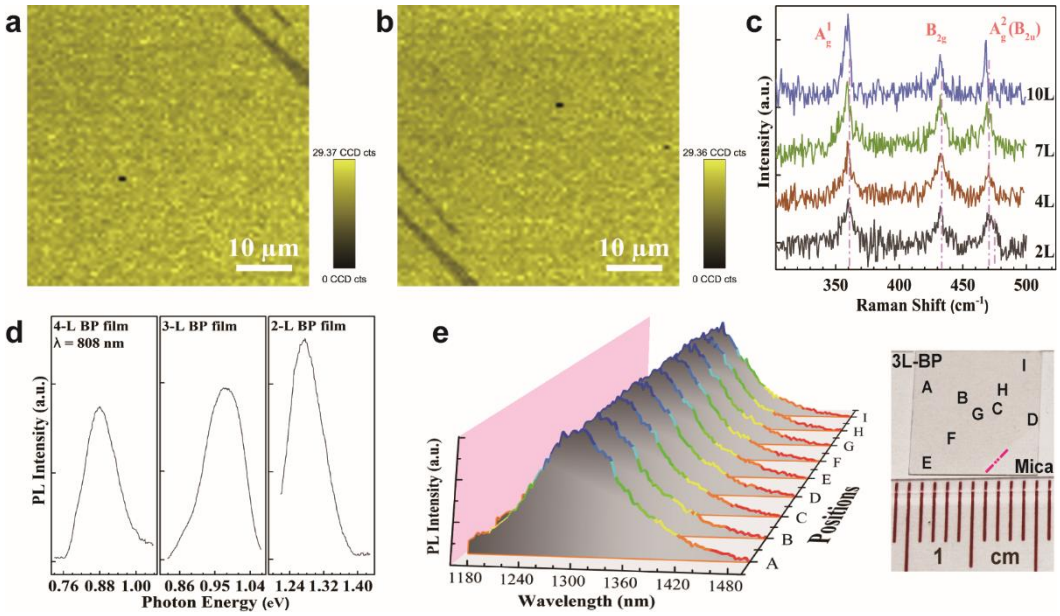

Fig. 2. Large-area homogeneity of centimeter-scale few-layer BP films. a, b, Raman mapping images on integrated intensity of BP A^2_g peak over two 60×60-μm regions of lower-left and upper-right area in optical micrograph image (Extended Data Fig. 6a), respectively. The signal-blank zones appear in the upper-right corner of **a** and the lower-left corner of **b** are caused by the same scratches. **c,** Raman spectra of few-layer BP. A slight left-shift is observed with increasing layer-number. For bilayer BP, the peak emerges next to A^2_g band can be traced back to the infrared active B_{2u} mode, further evidencing the bilayer nature of this sample[21]. **d,** PL spectra of few-layer BP films, indicating the layer-dependent property of intrinsic bandgap. **e,** PL line-scan mapping study performed on the selected nine distanced points belonging to two intersecting lines on top of a 3-layer BP film. Inset shows nine investigated positions on the wafer, and the pink dashed-line indicates the boundary between deposited BP-film and bare mica-substrate.

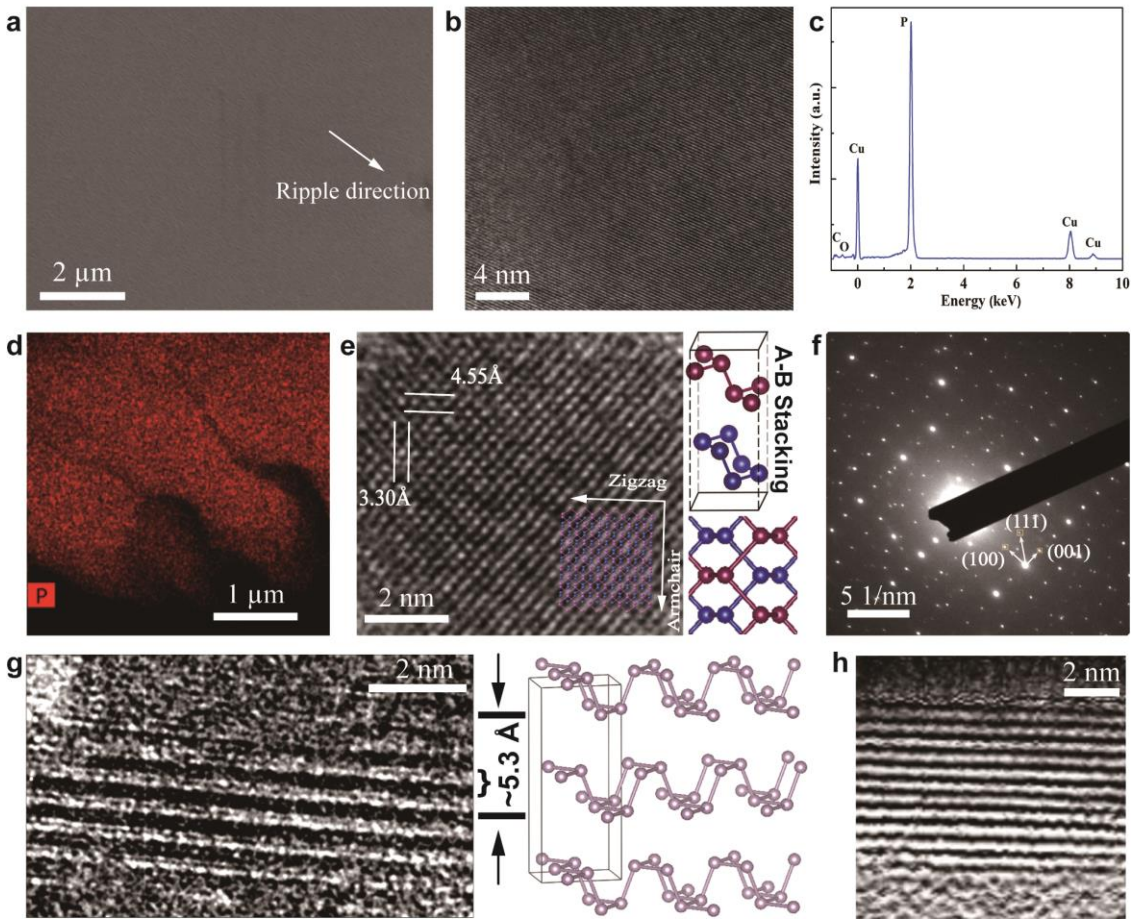

Fig. 3. Atomistic features of few-layer BP films. a, SEM image showing the surface morphology of BP film. Ripples in similar direction can be observed. **b,** Plan-view HR-TEM image of an 8-layer BP film. Defect-free atomic structure can be recognized. High elemental purity can be recognized via the related EDX spectrum in **c** and HAADF element-mapping image in **d**. **e,** Detailed HR-TEM image of BP lattice. The extracted lattice parameters match well with those of bulk BP single-crystal, and an orthorhombic symmetry with AB stacking mode can also be recognized, as illustrated by the inserted ball-stick schematics. Red and blue balls indicate the upper and lower BP layers within a bilayer BP structure, respectively. **f,** The corresponding SAED patterns. Crystalline features are demonstrated with zone-axis along [010] direction. **g, h,** Cross-sectional TEM images of BP films with various layer-number. The inset shows the corresponding atomic structure of BP layers, which possesses unique puckered structure with a double atomic layer within one BP layer.

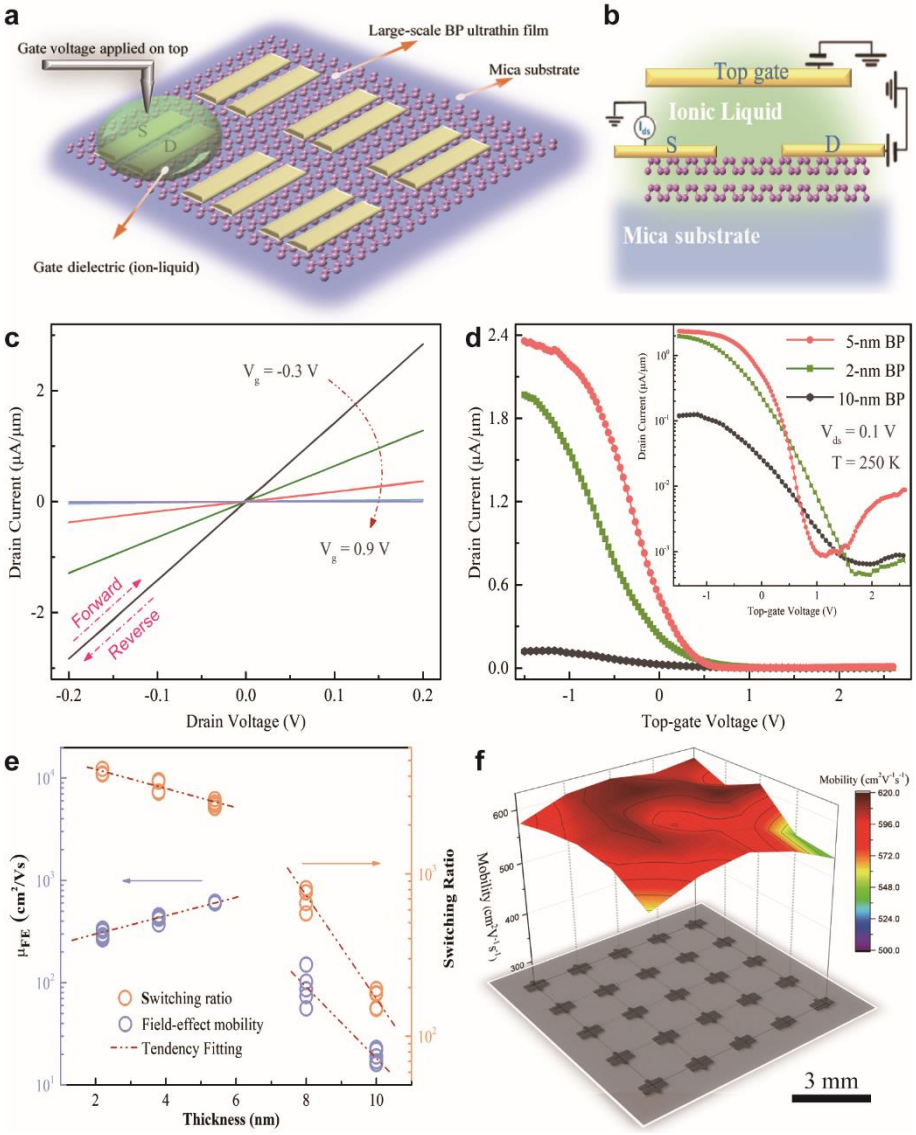

Fig. 4. Electrical performance of centimeter-scale few-layer BP. a, Schematic of arrayed top-gated FETs based on centimeter-scale few-layer BP grown on mica substrate. **b** shows the cross-section view of a single FET. **c,** A collection of I_d–V_{ds} curves for a FET based on 5-nm BP ultrathin film under different gate voltage. **d,** Transfer characteristics of the FETs based on 2-nm, 5-nm and 10-nm BP ultrathin films in linear scale at 250 K. The inset shows the same results in logarithmic scale. **e,** Field-effect mobility and switching ratio resulted from the FETs as a function of BP-film thickness based on **d** and further repetitive experiments. **f,** 3D color map of carrier mobility extracted from 25 FETs on the same BP sample, showing high uniform device performance. The optical image of arrayed devices on top of the BP sample with 1×1 cm^2 area is included in the figure.

Methods

Growth of wafer-scale few-layer BP films

Firstly, surface stripping was carried out on mica substrate before it was mounted in the growth chamber, which guarantees a fresh and spotless substrate surface for the subsequent BP deposition. Afterwards, the source (BP single crystal, *SMART-ELEMENTS*) and substrate were placed face to face in the chamber, with a separation distance of ~36 mm. The chamber was then pumped to an ultrahigh vacuum level of ~1.6×10^{-9} Torr, and the mica substrate was heated up to 300 ℃. Upon the KrF excimer pulsed laser (λ = 248 nm) with a repetition rate of 5 Hz and a laser fluence of 1.2 J/cm^2, plasma plume containing large BP clusters was generated from the target. The physical vapor containing ablated clusters was then transmitted towards the surface of mica substrate and few-layer BP film was formed under controlled substrate temperature. The mica substrates were kept rotating during the growing process to achieve uniform deposition, while the BP source was fixed to maintain the uniformity and stability of plasma plume. After the deposition, the temperature of as-synthesized BP films was immediately and rapidly decreased down to RT by venting dry N_2 gas into the growth chamber and moving the sample holder away from heater. To prove the effectiveness of the rapid-cooling approach, a comparison of cooling rates between natural and rapid cooling was experimentally performed, as exhibited in Extended Data Fig. 1, where the cooling rate is significantly promoted for rapid-cooling strategy. In order to avoid degradation of as-prepared few-layer BP films, transferring samples for subsequent studies was implemented using sealed containers filled with protection gas.

Bulk black phosphorus (BP) single crystal was used as the source material for the deposition to inhibit the ejection of heterogeneous large particles or droplets, which renders the formation of BP films with well-defined morphology. This laser-ablated ejecting model has been demonstrated for a wide variety of source materials in previous studies on laser ablation processing, especially those substances that can hardly form dense and uniform targets[27,28]. Regarding the substrate for the deposition, freshly exfoliated mica was used to facilitate epitaxial growth of BP film. Recently, mica substrate has been considered as a promising candidate for the vdW-epitaxial growth of two-dimensional (2D) materials. Owing to the 2D nature of mica, its freshly exfoliated surface possesses satisfactory atomic planeness and surface inertness, allowing a low migration barrier energy (E_m) for 2D material growth[29-33].

Growth of monolayer MoS_2 triangle

MoS_2 nanosheets of fine triangular shape were synthesized by CVD method. A powder mixture of 10 mg MoO_3 and 5 mg NaCl in a quartz boat was placed in the center of the quartz tube. 20 mg of sulfur powder was placed on the upstream of the furnace at 180 °C. Prior to crystal growth, the quartz tube was vacuumed below 6 Pa and flushed with Ar carrier gas. The furnace was then heated to the growing temperature (750 °C) with a ramp rate of 15 °C min^{-1} and held for 10 min before cooling down to RT naturally. Ar carrying gas with a flow rate of 60 sccm was used to facilitate crystal growth.

Model settings of MD simulations

MD simulation was performed using Large-scale Atomic/Molecular Massively Parallel Simulator (LAMMPS) to simulate the laser influence during PLD process. 4-layer BP with lateral dimension of 100Å × 100Å was modelled. Periodic boundary conditions were imposed along the in-plane x- and y-directions to eliminate the edge effect, and a 200 Å vacuum layer was applied along the out-of-plane z-direction. The Stillinger-Weber (SW) potential was implemented in the simulations to define the intra-layer P-P bonds. The parametrization of SW potential for phosphorene was based on ab initio valence force field (VFF) model by Jiang *et al*[34]. For the interlayer interactions between adjacent BP layers, the 12-6 Lennard-Jones (LJ) potential was employed by:

$$V(r) = 4\epsilon\left[\left(\frac{\sigma}{r}\right)^{12} - \left(\frac{\sigma}{r}\right)^{6}\right] \quad (1)$$

where r is the separation between two particles. The energy constant ϵ and distance constant σ are obtained from the universal force field[35], where ϵ = 0.0132 eV and σ = 3.695 Å. The cutoff distance for the LJ potential is set as 15 Å.

During the simulation, a time step of 0.5 fs was used to integrate the equations of motion. The initial configuration first undergoes energy minimization at 0 K with the conjugate gradient method. System equilibration was then carried out at 300 K with Nose-Hoover thermostats to release internal stresses in BP structure. Upon equilibration, the system was switched to micro-canonical (using NVE simulation, where N, V, and E refer to the number of particles, the volume, and the total energy, respectively) ensemble with constant volume and energy. To simulate the effect of laser heating, a constant heat

fluence was added to the surface BP-layers, while the position of the bottom BP-layers was fixed. With the effect of laser acting, the ablated phosphorus segments were extracted for BP-cluster formation.

During the formation process, the simulation box was reset to fixed boundary conditions along all directions. To simulate dynamic bond creation, a harmonic bond potential was defined according to the VFF model[36]. The bond-stretching and angle-bending potentials are can be described by:

$$V_r = \frac{1}{2}K_r(r - r_0)^2 \quad (2)$$

$$V_\theta = \frac{1}{2}K_\theta r_1 r_2(\theta - \theta_0)^2 \quad (3)$$

where K_r and K_θ are valence force constants; r_0 and θ_0 are equilibrium bond and angle, respectively. Accordingly, we used r_0 = 2.224 Å and K_r = 7.578 eV/Å^2 for bonds, θ_0 = 96.359° and K_θ = 0.818 eV/Å^2 for *Angle I* (*zigzag*), and θ_0 = 102.090° and K_θ = 0.710 eV/Å^2 for *Angle II* (*armchair*), respectively, in our simulations[36]. Notably, here we assume all the bonds in BP structure have the same length and stretching parameters. The LJ potential was adopted to define the vdW force among all the phosphorus atoms. To guarantee the ablated segments reaching steady state, the system was equilibrated before data collection. OVITO package was used to visualize and analyse the atomistic simulation data. The RDF was obtained by averaging multiple measurements in the steady state.

Output analysis of MD simulations

In consistence with the experiments, five typical laser-fluence conditions (0.8, 1.2, 2.0, 2.8 and 3.8 J/cm^2) were used to investigate the atomic structure evolution under laser heating through MD simulation. From the output results (Extended Data Fig. 5), it can be recognized that the formation of large phosphorus clusters only occurs under relatively low laser-energy. Both 0.8 and 1.2 J/cm^2 laser fluences render the formation of phosphorus clusters back to BP clusters, verified by the characteristic puckered structure of BP. At a laser fluence of 0.8 J/cm^2, however, the amount of ablated phosphorus is essentially small, which is not applicable for large-scale film growth. At a laser fluence of 1.2 J/cm^2, many of the ablated phosphorus segments retain the unique structure of BP, thus yielding considerable amounts of phosphorus clusters with BP characteristics. Under this condition, larger BP clusters exhibit dense and uniform distribution in the plasma cloud, rendering the formation of large-scale BP films after a vapor-phase transmission process. It is worth noting that after simulations on the laser action and cluster evolution, the simulation system presents high-temperature and high-pressure state of more than 10^3 K and 10^9 Pa, respectively, which are highly desirable for BP-clusters formation. Notably, due to the size of simulation box, we can only study the molecular dynamics evolution within a small region, though the actual situation should be able to produce higher temperature and pressure in the plasma region. As the laser fluence increases to higher levels, the ablated P ions fail to order themselves into BP structures due to the excessively high kinetic energy. The amount of resulting BP-like clusters dramatically decreased, while the discretely scattered P ions can be observed. As the laser fluence further increases to 3.8 J/cm^2, the energy of the system

is extremely high, and the ions oscillated dramatically. Therefore, the plasma mainly consists of highly disordered P ions in random distribution and barely any cluster can be observed.

To further validate the molecular dynamic process, the RDF, g(r) was investigated for structural characterization. RDF describes the probability of finding an atom as a function of distance from the reference atom[17]. Typically, the sharp peaks represent fixed distances characterizing the crystalline nature of the material while smooth features represent disordered or amorphous state of the material. Fig. 1g in the main text depicts the RDF curves extracted from MD simulation processes with varying laser fluence, from which five characteristic peaks can be recognized as fingerprints to verify the formation of BP clusters. The first peak *I* centered at ~2.23 Å represents the covalent bonding distance between adjacent P atoms, which corresponds to the nearest neighbor (e.g.,1-2, 2-4) in BP structure[18]. This peak is a two-body interaction and can be observed for all laser conditions, indicting a certain trend of evolution towards BP clusters. In contrast, another peak centered at ~3.40 Å is only observed under lower-laser-fluence conditions. This broad peak contains information about three characteristic distances, *II*, *III* and *IV*, indicating the three-atom zigzag, four-atom armchair, and three-atom armchair features of BP, respectively[18]. They are responsible for the fingerprints of BP allotrope involving characteristic many-body terms, which renders the distinction between different phosphorus allotropes. The absence of these three characteristics under high laser-energy conditions implies that the formation of BP clusters is irrupted.

The flat peak centered at ~4.15 Å represents the van der Waals interaction between P atoms without chemical bonding[17,18]. This peak increases dramatically under high laser-energy conditions, indicating considerable amount of free P atoms in the system. Interestingly, the radial distribution after 10 Å exhibits a higher intensity with higher energy conditions, further evidencing the random distribution and highly disordered of P ions caused by higher laser-energy.

To further validate the characteristic fingerprints of BP structure, the broad peak centered at ~3.40 Å was differentiated and imitated into three individual peaks, *II*, *III*, and *IV*, representing the second neighbor (e.g.,1-3, 5-7; d_2 ≈ 3.31 Å), third neighbor (e.g., 2-6, 2-8; d_3 ≈ 3.45 Å), and fourth neighbor (e.g., 2-5, 4-6; d_4 ≈ 3.53 Å), respectively (see Fig. 1h in the main text). These characteristic peaks can be explained by the VFF model for BP structure[18]. The second and fourth neighbors are related to three-body interactions which involve *Angle I (zigzag)* and *Angle II (armchair)*, respectively (see Equation No. 2). The third neighbor is related to four-body interaction, which contains a sequence of four atoms with a full armchair structure (e.g. 2-4-5-6). To characterize the formation of BP-like clusters, the peak intensities of two-body interaction and many-body interaction for zigzag and armchair configurations were extracted. As shown in Extended Data Fig. 5f, all the RDF peaks have highest proportions at 1.2 J/cm^2, especially for peaks related to the unique many-body interactions in BP structure. It means that the ratio of BP-like clusters reaches maximum under this laser fluence, which is consistent with our experimental findings.

Accordingly, one can conclude that a laser fluence of ~1.2 J/cm is optimal for BP synthesis in our PLD process.

Material characterization methods

Raman investigations were carried out by a high-resolution confocal μ-Raman system (Horiba, HR 800) equipped with 488-nm laser source (spot size: 1 μm). To preserve the crystalline structure of BP samples, the laser power through a × 100 objective was controlled at a low level of ~1 μW. The thickness and surface morphology of few-layer BP films were studied by a commercial atomic force microscope (Asylum Research MFP-3D). PL measurement was conducted by an FLS920P Edinburgh Analytical Instrument apparatus equipped with 808-nm diode laser (MDL-808 nm) as an excitation source. The crystal structure of as-prepared sample was characterized by X-ray diffraction (Rigaku smart lab 9 kW, Japan) with Cu Kα radiation (λ = 1.5406 Å). BSE and SEM images were obtained from Tescan VEGA3 Scanning Electron Microscope, with the electron-voltage controlled at 5 kV. The micro-structures and chemical compositions of as-prepared BP films were investigated by field-emission scanning transmission electron microscopy (FE-STEM, JEOL Model JEM-2100F) equipped with an energy dispersive X-ray spectroscopy, using 100-kV accelerating voltage and 0.3-s exposure time. Specimens for HR-TEM measurements were prepared by polystyrene (PS)-mediated transfer approach with ethanol-assisted lift-off. Specimens for cross-section TEM measurements were obtained by applying focused ion-beam (FIB, JEOL JIB-4500) milling and lift-off technique. All the obtained samples were

transferred onto copper grids for TEM characterization.

Device fabrication methods

Followed by the deposition and the rapid-cooling process, mica-based few-layer BP films were covered with hard-mask templates (made of highly purified molybdenum) with designed patterns and transferred into the electron-beam deposition (EBD, Denton Vacuum E-beam Explorer System) chamber with dry N_2 protection. Then, 10-nm-Pd/40-nm-Au metal contact multilayer was deposited on the top of BP films to form the source, drain, and gate electrodes. The growth rates of Pd and Au layers were carefully controlled at 0.2 and 0.7 Å/s, respectively, to avoid potential damage on the surface of BP layers. Typically, the channel length (L_{ch}) of the obtained FETs is 40 μm, while the channel width (W_{ch}) is 400 μm. Prior to the measurement, one droplet of ionic liquid (IL, using DEME-TFSI, Sigma Aldrich 727679) was carefully positioned on the top of the construction using a micro-manipulator under optical microscope, covering source, drain and gate electrodes. After dehydration, an IL gate-dielectric layer was formed by self-assembly, yielding a top-gated FET.

Device characterization methods

After fabrication, the devices were then cooled down to 250 K and hold for a few minutes in vacuum of 6×10^{-7} Torr before being characterized, so as to freeze water in the ionic liquid. Although the applied voltage is relatively low in our experiment, this designed low-temperature test can further exclude the possibility of water electrolysis

during the measurement, which may cause degradation of intrinsic electrical properties of BP. Device characterization was carried out at 250 K by using Keithley 4200 Semiconductor Parameter Analyzer equipped with a probe station connected with vacuum chamber, liquid-helium cryogenic test platform, micro-manipulator with 5-μm tips, and optical microscope. Additionally, because the semiconductor devices are usually operated at RT in real applications, we also make a further step to study the RT performance of our BP-based FETs (Extended Data Fig. 9 a-b). Since the theoretical electrolytic voltage of water is around 1.5 V (greater than 2.1 V if heat balance is considered), the performance of our devices was verified within a voltage range less than this critical value, that is, the voltage that ensures the water is not ionized. The characterization was conducted in dark environment to prevent ambient light influence on the measured electrical properties of BP.

Capacitance-density determination of ionic-liquid

To guarantee the accuracy and reliability of electrical performance measurements, relatively stable and conventional MoS_2 nanosheets were employed for comparison. Analogues to the structure of BP-based top-gated FETs, we constructed this MoS_2-based device using chemical vapor deposition (CVD)- grown triangular MoS_2 samples on 300 nm SiO_2/Si substrates. Extended Data Fig. 8 shows the determination process of capacitance density of the ionic liquid droplet. As shown in Extended Data Fig. 8a, the underlying silicon layer acts as back-gate electrode of the FET by using 300-nm SiO_2 as the dielectric, while the Pd/Au electrodes deposited on top of the MoS_2 act as

the source, drain and top gate by using ionic-liquid that dropping on top of these three electrodes as the dielectric. When drain voltage (V_{ds}) and top-gate voltage (V_{tg}) are applied on the FET, the transfer characteristic curve can be obtained (Extended Data Fig. 8b). Extended Data Fig. 8c exhibits the evolution of the FET output curve when back-gate voltage (V_{bg}) is applied, in which the most affected parameter is the threshold voltage (V_{th}) in I_{ds}-V_{tg} curves. As V_{bg} gradually increases from 0 to 30 V, the corresponding V_{th} systematically shifts to the negative V_{tg} position, while the slope of the I_{ds}-V_{tg} curves within the linear work-region remains nearly constant. The estimation of the capacitance of ion-liquid ($C_{tg\text{-}IL}$) is based on the change of ΔV_{th} in response to the variation of ΔV_{bg}:

$$C_{tg-IL}/C_{bg} = \Delta V_{bg}/\Delta V_{th} \quad (4)$$

where C_{bg} = 1.2 × 10^{-8} F/cm^2 is the capacitance-per-unit-area of the SiO_2 (back-gate dielectric), and $\Delta V_{bg}/\Delta V_{th}$ = 120 is extracted through linear fitting (see Extended Data Fig. 8d). Accordingly, the capacitance of the ion-liquid droplet per unit area is estimated to be $C_{tg\text{-}IL}$ ~ 1.44 × 10^{-6} F/cm^2 (Extended Reference No. 37).

Calculation of the field-effect mobility

The field-effect carrier mobility (μ_{FE}) of the large-scale few-layer BP films can be extracted from transport characteristic curves of the top-gated FETs:

$$\mu_{FE} = \frac{L}{WC_{tg-IL}V_{ds}}\frac{dI}{dV} \quad (5)$$

where L is the channel length (40 μm), W is the channel width (400 μm), $C_{tg\text{-}IL}$ is the capacitance density of ionic liquid (1.44 × 10^{-6} F/cm^2), V_{ds} is the applied drain voltage,

and *dI/dV* is the field-gating efficiency obtained by matching the slope of the curve within the linear work-region. Due to the fixed dosage of ionic liquid employed in the device fabrication, the contributing capacitance density used for mobility calculation can be considered as a constant[37].

References for Methods and Extended Data

27 von Wenckstern, H. *et al.* Continuous composition spread using pulsed-laser deposition with a single segmented target. *Cryst. Eng. Comm.* **15**, 10020 (2013).

28 Li, Y., Yao, X. & Tanabe, K. Improved surface morphology of $NdBa_2Cu_3O_{7-\delta}$ films grown by pulsed laser deposition using a large single crystal target. *Physica C Supercond.* **304**, 239-244 (1998).

29 Huang, W. *et al.* Controlled Synthesis of Ultrathin 2D β-In_2S_3 with Broadband Photoresponse by Chemical Vapor Deposition. *Adv. Funct. Mater.* **27**, 1702448 (2017).

30 Wen, Y. *et al.* Epitaxial 2D PbS Nanoplates Arrays with Highly Efficient Infrared Response. *Adv. Mater.* **28**, 8051-8057 (2016).

31 Zhou, Y. *et al.* Epitaxy and Photoresponse of Two-Dimensional GaSe Crystals on Flexible Transparent Mica Sheets. *ACS Nano* **8**, 1485-1490 (2014).

32 Koma, A. Van der Waals epitaxy for highly lattice-mismatched systems. *J. Cryst. Growth* **201**, 236-241 (1999).

33 Lui, C. H., Liu, L., Mak, K. F., Flynn, G. W. & Heinz, T. F. Ultraflat graphene. *Nature* **462**, 339-341 (2009).

34 Jiang, J. W. Parametrization of Stillinger-Weber potential based on valence force field model: application to single-layer MoS_2 and black phosphorus. *Nanotechnology* **26**, 315706 (2015).

35 Rappé, A. K., Casewit, C. J., Colwell, K. S., A., G. I. W. & Skiff, W. M. UFF, a Full Periodic Table Force Field for Molecular Mechanics and Molecular Dynamics Simulations. *J. Am. Chem. Soc.* **114**, 10024–10035 (1992).

36 Kaneta, C., Katayama-Yoshida, H. & Morita, A. Lattice dynamics of black phosphorus. *Solid State Commun.* **44**, 613-617 (1982).

37 Perera, M. M. *et al.* Improved Carrier Mobility in Few-Layer MoS_2 Field-Effect Transistors with Ionic-Liquid Gating. *ACS Nano* **7**, 4449-4458 (2013).

38 De Yoreo, J. J. & Vekilov, P. G. Principles of Crystal Nucleation and Growth. *Rev. Mineral. Geochem.* **54**, 57-93 (2003).

39 Wang, S. *et al.* Shape Evolution of Monolayer MoS_2 Crystals Grown by Chemical Vapor Deposition. *Chem. Mater.* **26**, 6371-6379 (2014).

40 Kondo, H., Hamada, N. & Wagatsuma, K. Determination of phosphorus in steel by the combined technique of laser induced breakdown spectrometry with laser induced fluorescence spectrometry. *Spectrochim. Acta Part B: At. Spectrosc.* **64**, 884-890 (2009).

607 41 Zhang, B., Ling, P., Sha, W., Jiang, Y. & Cui, Z. Univariate and Multivariate
608 Analysis of Phosphorus Element in Fertilizers Using Laser-Induced Breakdown
609 Spectroscopy. *Sensors* **19**, 1727 (2019).

610 42 Na, J. *et al.* Few-Layer Black Phosphorus field-effect transistors with Reduced
611 Current Fluctuation. *ACS Nano* **8**, 11753-11762 (2014).

612 43 Yang, Z. *et al.* Field-Effect Transistors Based on Amorphous Black Phosphorus
613 Ultrathin Films by Pulsed Laser Deposition. *Adv. Mater.* **27**, 3748-3754 (2015).

614 44 Yue, D. *et al.* Passivated ambipolar black phosphorus transistors. *Nanoscale* **8**,
615 12773-12779 (2016).

616 45 Yasaei, P. *et al.* High-Quality Black Phosphorus Atomic Layers by Liquid-
617 Phase Exfoliation. *Adv. Mater.* **27**, 1887-1892 (2015).

618 46 Lu, W. *et al.* Plasma-assisted fabrication of monolayer phosphorene and its
619 Raman characterization. *Nano Res.* **7**, 853-859 (2014).

Acknowledgements

This work was supported by the grants from the National Natural Science Foundation of China (No. 51972279) and Research Grants Council of Hong Kong (GRF No. PolyU 153025/19P, PolyU 153039/17P and CRF no. C7036-17W) and PolyU Grant (1-ZVGH).

Author contributions

J.H., Z.W. and X.H.C. conceived the original idea and designed the experiments. J.H., S.P.L. and X.H.C. supervised the projects. Z.W. and B.Z. developed the synthesis techniques and fabricated the samples. Y.L. performed MD simulations. Y.Z. conducted TEM and EDX experiments. Z.W. and R.D. performed other physical characterizations, including AFM, BSE, PL, Raman, SEM, and XRD studies, and analyzed the results. Z.W. and Z.Y. fabricated FET devices and investigated the electrical properties. Z.W., Y.L., X.H.C. and J.H. co-wrote the paper and all authors commented on it.

Competing interests

The authors declare no competing interests.

Additional information

Correspondence and requests for materials should be addressed to X.H.C. or J.H.

Peer review information

Reprints and permissions information is available at http://www.nature.com/reprints.